Supplementary Material: EnGeoMAP 2.0—Automated Hyperspectral Mineral Identification for the German EnMAP Space Mission

Christian Mielke, Christian Rogass, Nina Boesche, Karl Segl and Uwe Altenberger

Here additional data and figures are presented that should help the reader to better understand the facts presented in the article in addition to the figures and tables already present in the article itself. This was a necessary step to preserve the compactness of the article.

Supplement 1

Below follows a pseudocode description of the Geometric Hull [1] algorithm highlighting the most important steps. Figure S1 shows the process of mineral zonation extraction in form of a flow chart.

```
  Geometric_Hull_Feature_Def(Input_Spectrum):

Gen_spectrum=Generic_1nm_Interpolation(Input_Spectrum, Method='Cubic Splines')
First_filt_step=Filter_Boxcar(Gen_Spectrum, boxcar_length='10% of Gen_spectrum')
Second_filt_step=Filter_Boxcar(First_filt_step, boxcar_length='10% of Gen_spectrum')
Third_filt_step=Filter_Boxcar(Gen_Spectrum, boxcar_length='2% of Gen_spectrum')
Fourth_filt_step=Filter_Boxcar(Third_filt_step, boxcar_length='2% of Gen_spectrum')
Aux1=Stdev(Second_filt_step- First_filt_step)
Aux2=Stdev(Fourth_filt_step- Third_filt_step)
If Aux1>=Aux2:
   Aux3= First_filt_step/Second_filt_step
Else:
Aux3= Third_filt_step/Fourth_filt_step
Peaks=Extract_Absorption_Peaks(Aux3)
Peak_Indices=Get_Indices(Absorption_Peaks)
Lower_Hull=Interpolate_Linear(Gen_Spectrum,Peak_Indices)
Segments=(Gen_Spectrum-Lower_Hull)
For each Segment in Segments:
Nodes=Get_Indices_of_Maximum(Segment)
Preliminary_Hull=Interpolate_Linear(Input_Spectrum,Nodes)
Hull=Iterate_over_Segments_unitl_Final_Hull_is_Found(Nodes, Gen_Spectrum)
Feature_Depth_Absolute, Feature_Depth_Relative =Hull_Removal(Hull,Gen_Spectrum)

Return (Hull, Feature_Depth_Absolute, Feature_Depth_Relative)
```

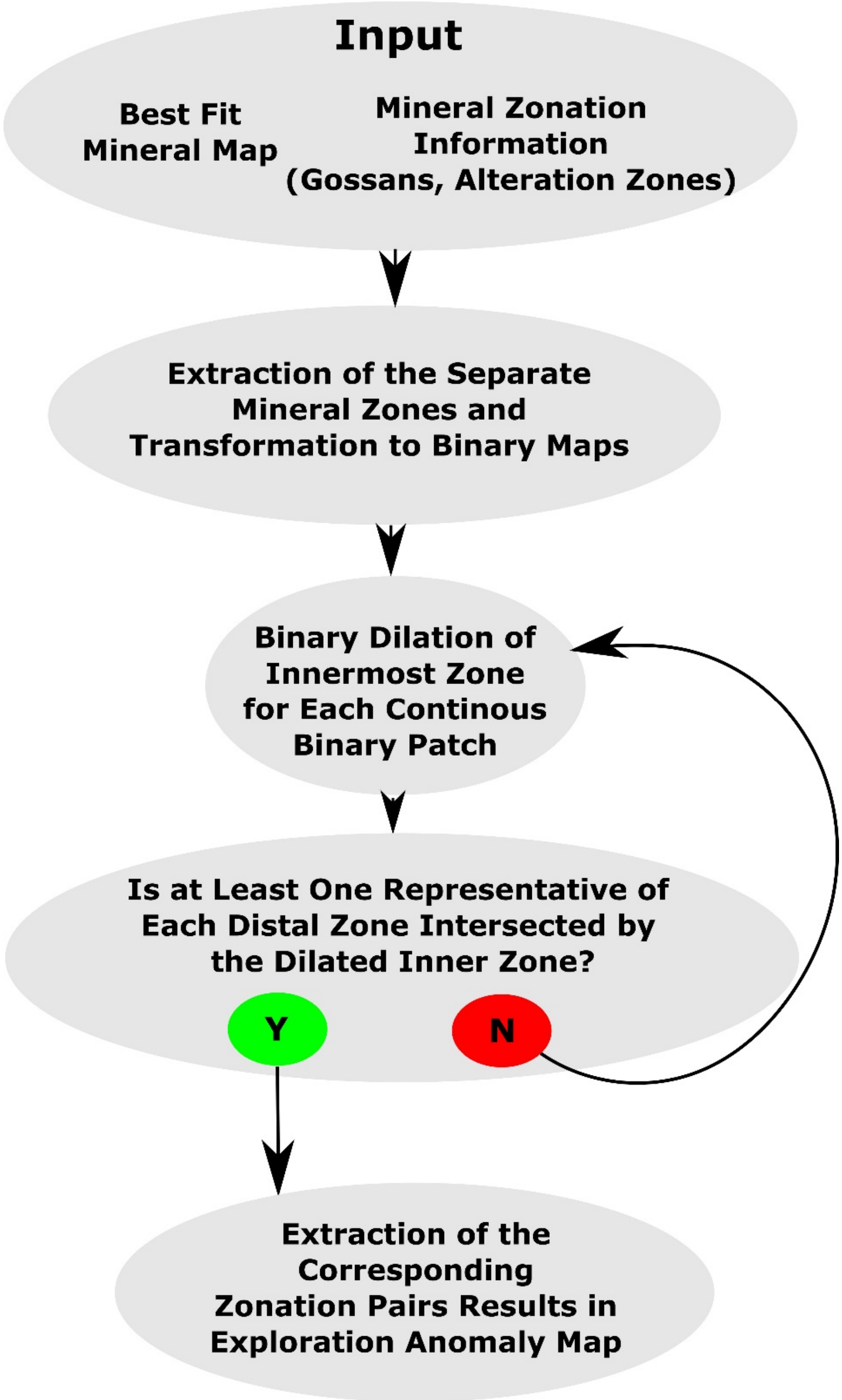

Figure S1. Flowchart showing the process of automated mineral zonation extraction.

Supplement 2

Supplement FigureS2 shows the characteristic absorption features defined for entries of the GFZ spectral library [2].

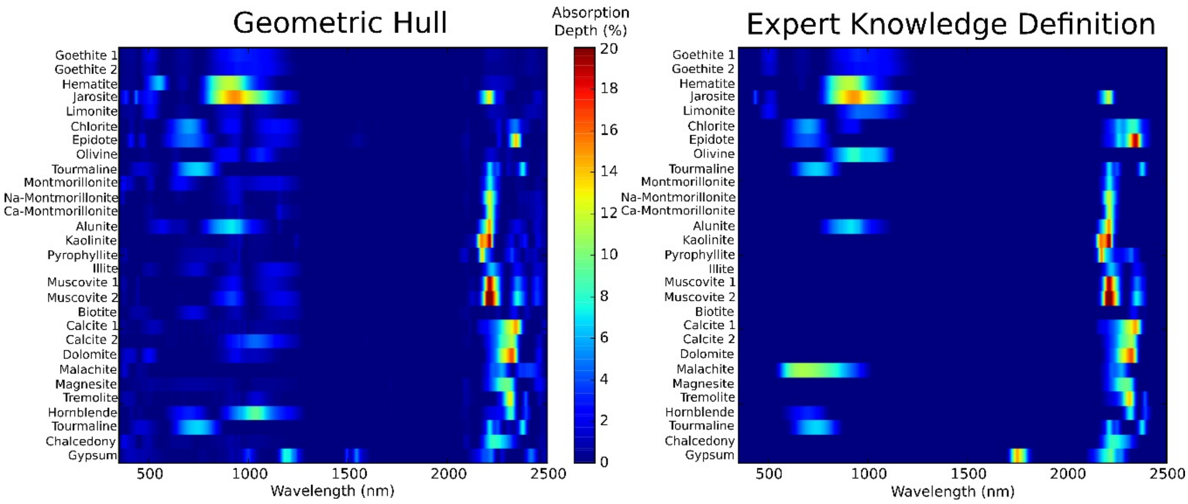

Figure S2. Characteristic absorption features of minerals in the solar reflective region extracted manually by expert knowledge based feature definition (**right**) and by the fully automated geometric hull technique (**left**). Spectral entries belong to the GFZ spectral library of Papenfuß (2015) [2].

Supplement 3

Correlation and Normalized Differential Vegetation Index (NDVI) [3] results for the Rodalquilar mineral deposit site. The NDVI is shown in Figure S3. The correlation coefficient to dry and green vegetation is shown in Figure S4. The spatial correlation between the vegetation pattern in Figure S3 and Figure S4 is obvious and demonstrates the capabilities of EnGeoMAP 2.0 for the detection of vegetation. The linear correlation to the features of the alunite reference spectrum is shown in Figure S5.

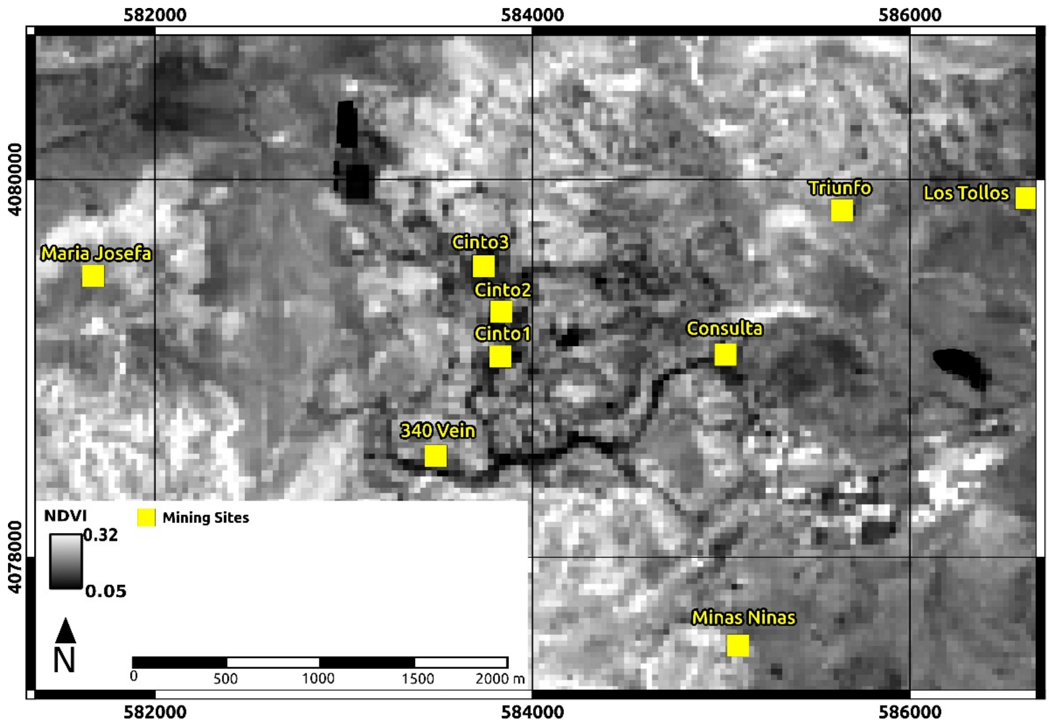

Figure S3. NDVI result for the Rodalquilar mineral deposit site.

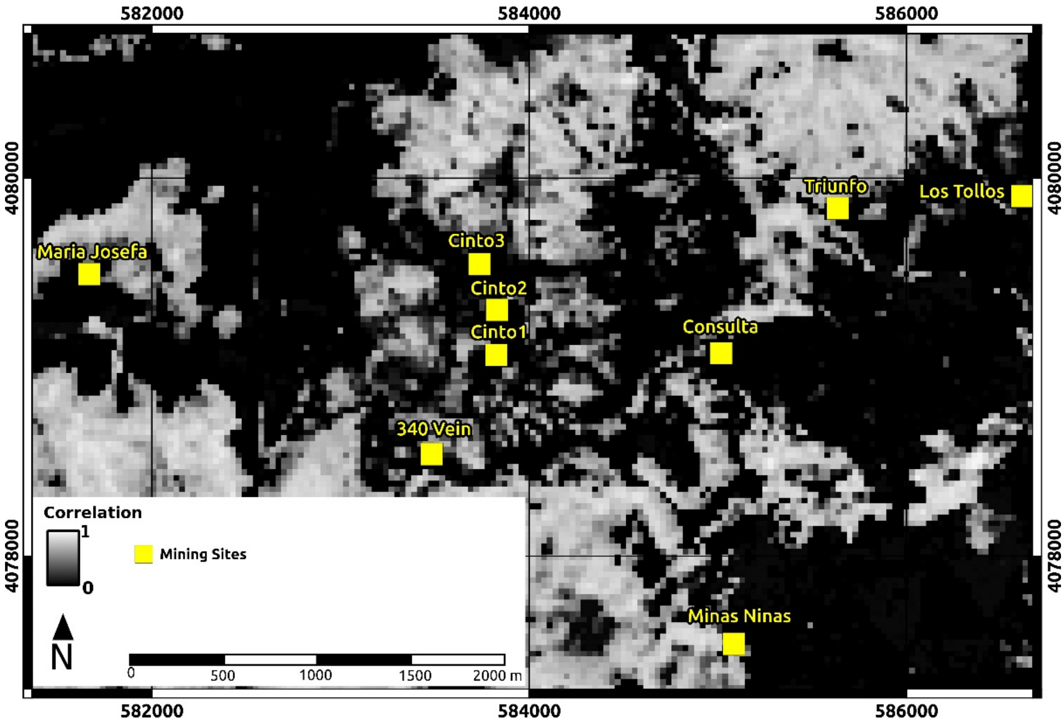

Figure S4. Correlation coefficient between the spectrum dry and green vegetation and the simulated EnMAP data for the Rodalquilar mineral deposit site.

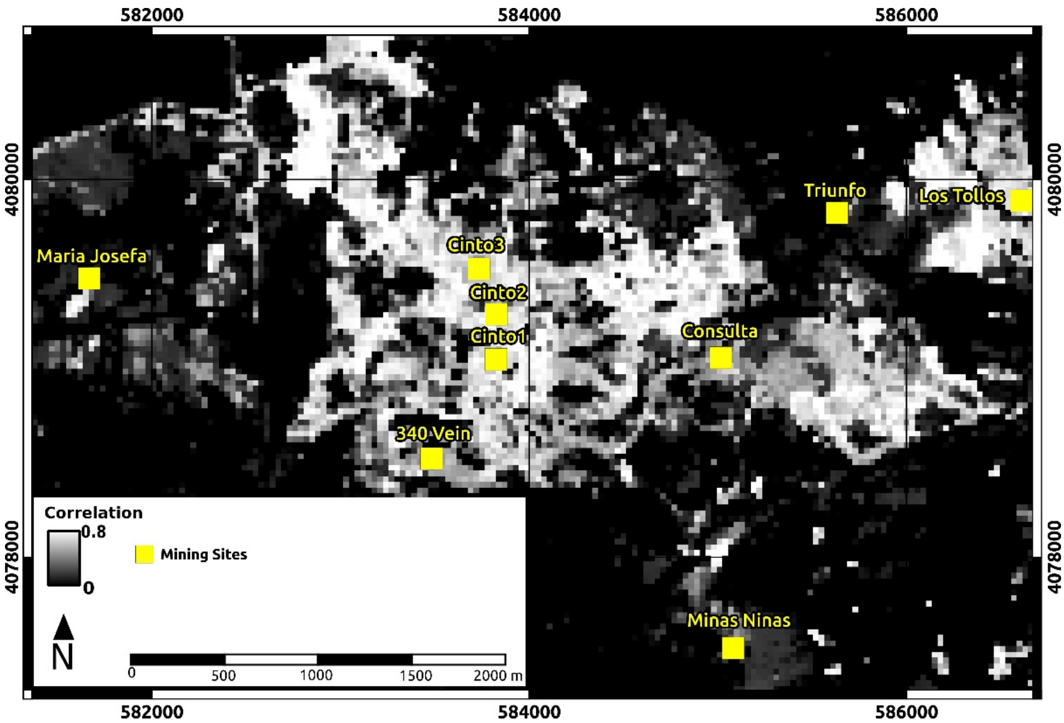

Figure S5. Correlation coefficient between the alunite reference spectrum and the simulated EnMAP data for the Rodalquilar mineral deposit site.

Supplement 4

Correlation and Normalized Differential Vegetation Index (NDVI) [3] results for the Haib river mineral deposit site. The low NDVI values in Figure S6 show that the Haib river area is an arid area with little vegetation, as also shown in Figure S7. Figure S8 shows that parts of the inner Haib river deposit are highly correlated with muscovite. Outer parts of the Haib river area show a high correlation with epidote illustrated in Figure S9. This can be interpreted as the innermost quartz-sericite zone and the outermost epidote, chlorite, calcite zone that have been described by Minnit [4] and Barr and Reid [5].

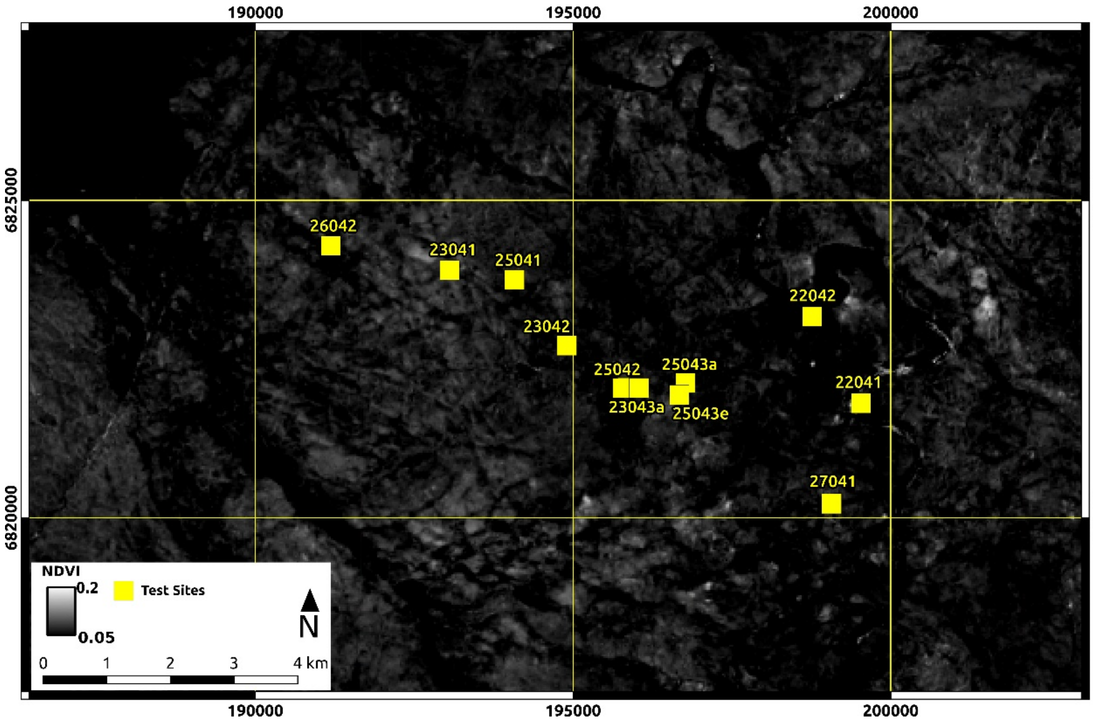

Figure S6. NDVI result for the Haib River mineral deposit site.

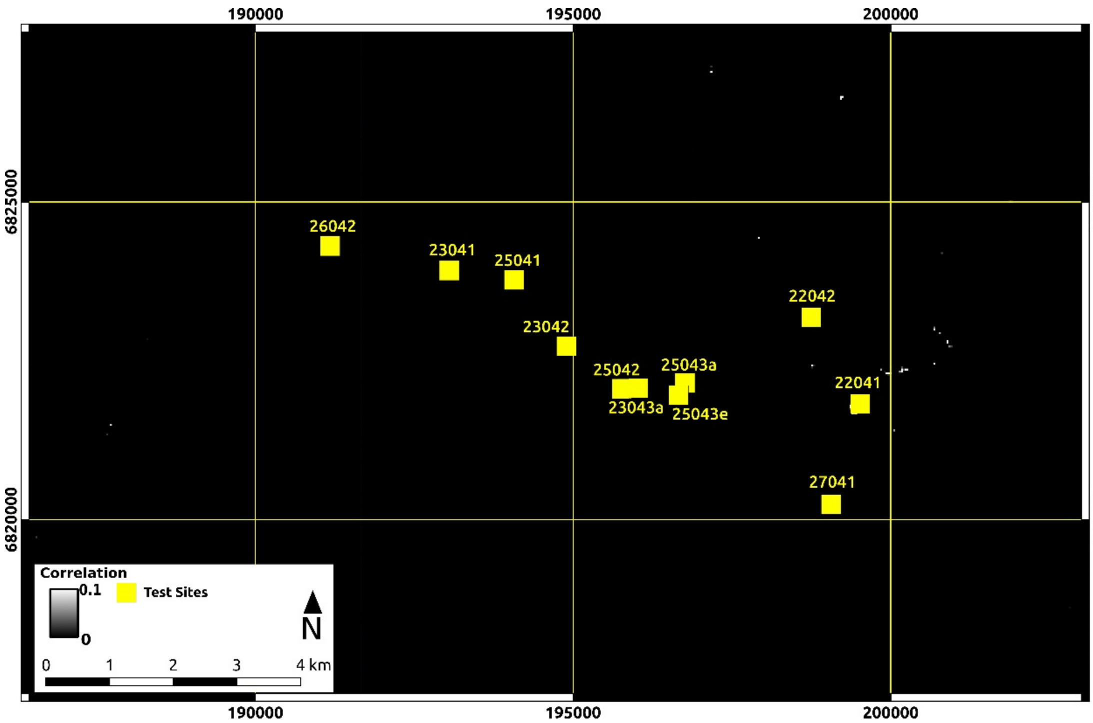

Figure S7. Correlation coefficient between the spectrum dry and green vegetation and the simulated EnMAP data for the Haib river mineral deposit site.

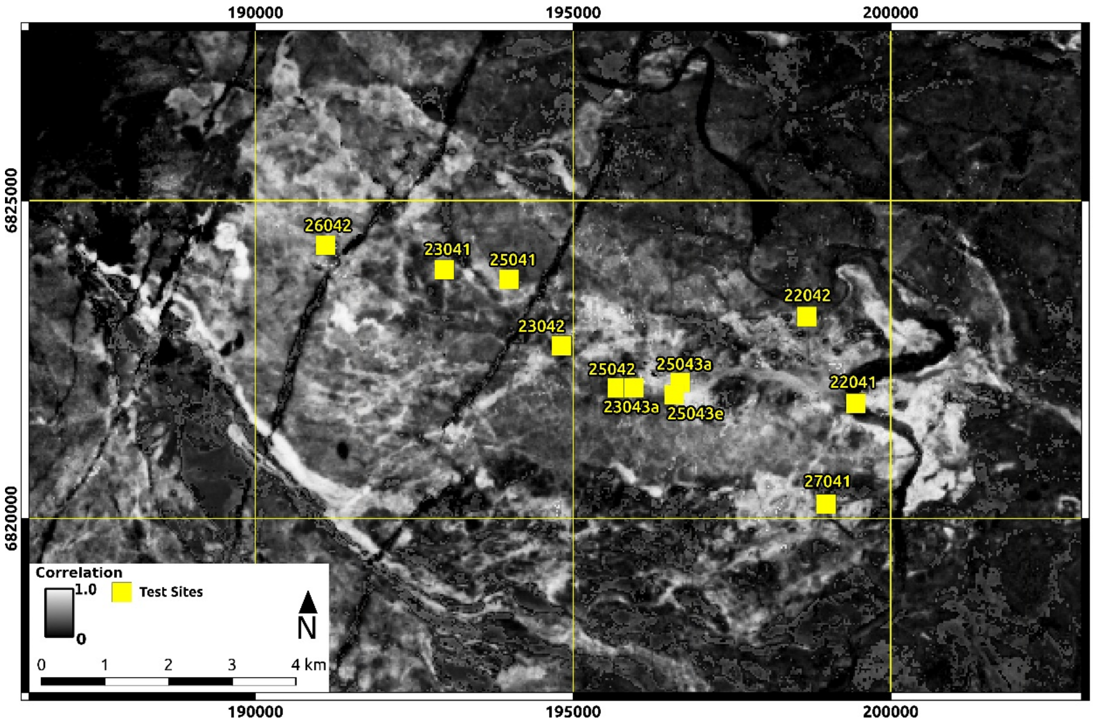

Figure S8. Correlation coefficient between the spectrum muscovite and the simulated EnMAP data for the Haib river mineral deposit site.

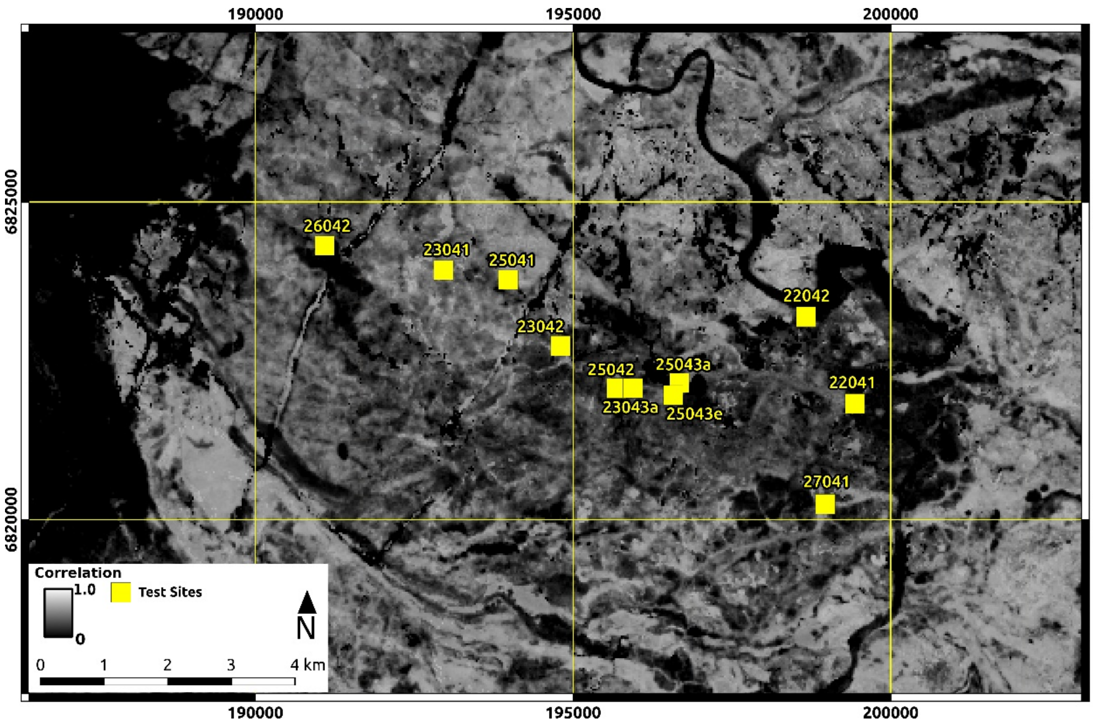

Figure S9. Correlation coefficient between the spectrum epidote and the simulated EnMAP data for the Haib river mineral deposit site.

Supplement 5

S5.1. Results from the Rodalquilar Deposit Sites

Results from Hyperion data are shown in Figures S10 and S11. The two major alteration centers around the Cinto deposit and around Los Tollos are also visible due to the presence of alunite and jarosite. However, there are large areas where no fit was possible. It was not possible to match the image spectrum at these locations to a library spectrum. Therefore, no classification result could be achieved in these areas. This is due to the lower SNR of the Hyperion data [6] if compared to EnMAP [7]. Therefore, a large proportion of the spectral absorption information has to be excluded from the EnGeoMAP 2.0 analysis. Figures S12 and S13 show the Hyperion results if a fixed user defined threshold is applied for a minimum feature depth of at least 2% in the VNIR and 3% in the SWIR. The area around the two major alteration zones is also visible in the mapping results using a user defined threshold. The main difference is the spatial distribution of green and dry and green vegetation as well as the presence of kaolinite in the material map of S12. This shows that the main alteration centers can also be found with Hyperion in both mineral maps. The greater abundance of calcite instead of kaolinite in the center of the Rodalquilar mining region in Figure S10 can be attributed to the aforementioned low SNR of Hyperion in the SWIR of 40 [6]. Furthermore, Hyperion data beyond 2335 nm had to be excluded from the analysis due to the rapidly increasing noise in the image spectra beyond this point.

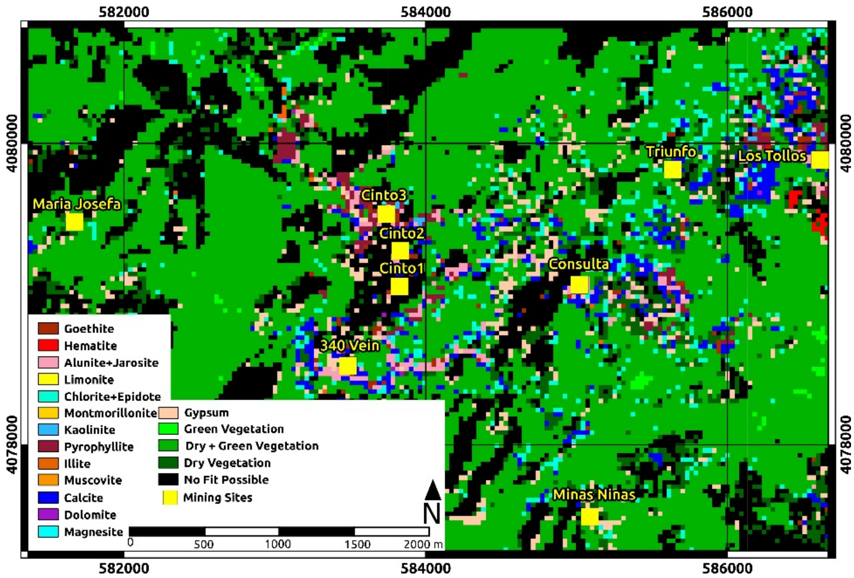

Figure S10. EnGeoMAP 2.0 result calculated from Hyperion data (EO1H1990342003060110KZ) using sensor specific absorption depth thresholding.

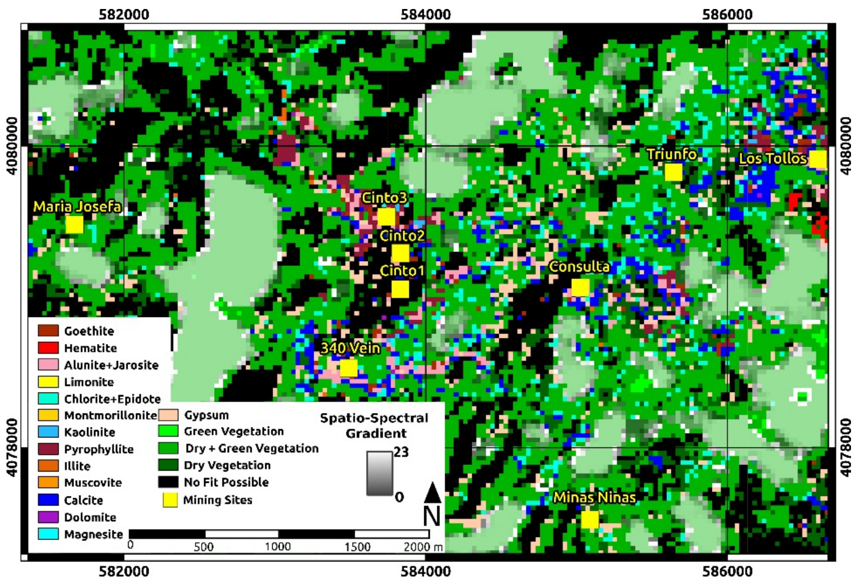

Figure S11. EnGeoMAP 2.0 result calculated from Hyperion data (EO1H1990342003060110KZ) using sensor specific absorption depth thresholding. With an overlay of the spatio-spectral gradients and prominent gradient edge pixel (non-transparent rim pixel around the gradient patches).

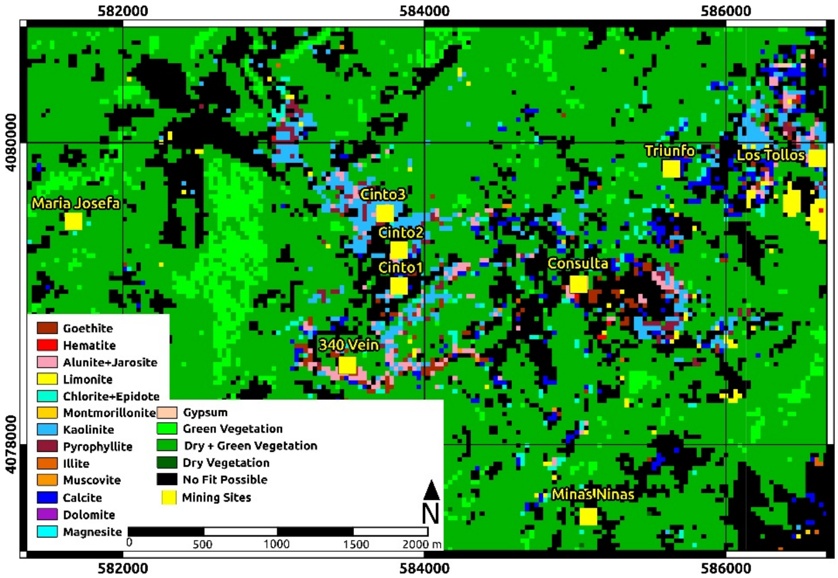

Figure S12. Material map using a user defined threshold of at minimum 2% feature depth until 1000 nm, and of at minimum 3% feature depth from 1000 nm on.

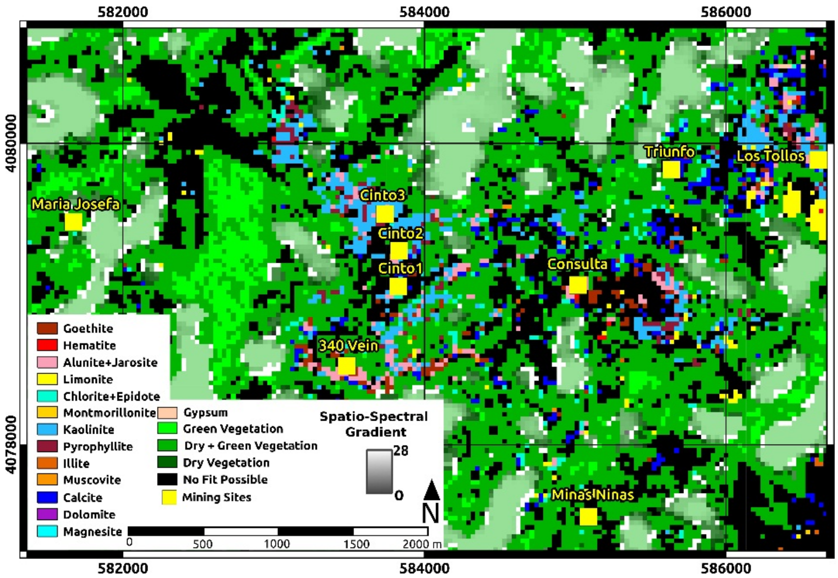

Figure S13. Material map using a user defined threshold of at minimum 2% feature depth until 1000 nm, and of at minimum 3% feature depth from 1000 nm on. The semi-transparent overlay shows the spatio-spectral gradient. Prominent gradient edge pixel shown as non-transparent rim pixel around the semi-transparent gradient patches.

S5.2. Results from the Haib River Deposit Sites

Figures S14 and S15 show no epidote or chlorite in the EnGeoMAP 2.0 results in contrast to Figures 13 and 14. This is due to the low SNR of Hyperion in the spectral region beyond 2000 nm, where epidote and chlorite have major characteristic absorption features as shown in Figure S2. In addition to that the image scenes were acquired with an "aging" sensor more than 10 years after the initiation of the extended mission period of EO-1 [8] unlike the Hyperion scenes of Rodalquilar, which were acquired in the beginning of 2003. This may also cause the detection of only those materials with a strong absorption depth contrast, like for example jarosite, montmorillonite, muscovite as illustrated in Figure S2. Nevertheless, the jarosite rich zones between 22042 and 22041 and the jarosite rich zone west of 27041 can be detected. Also prominent green and dry vegetation patches in the dry Haib River bed can be detected. Despite these problems it must be stated that a part of the gossan zone around 26042 can be identified via the presence of hematite, goethite and jarosite. This can also be seen in the center of the mineral deposit near 25042 and 23043a.

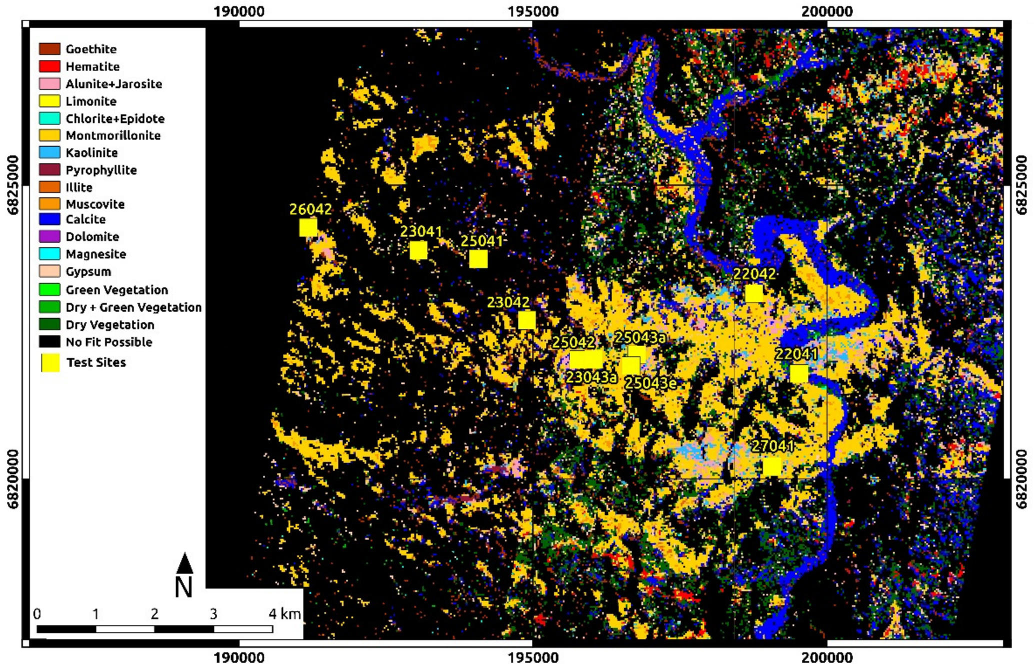

Figure S14. EnGeoMAP 2.0 result calculated from Hyperion data (EO1H1760802013267110KF and EO1H1760802014013110PF), using sensor dependent absorption depth thresholding.

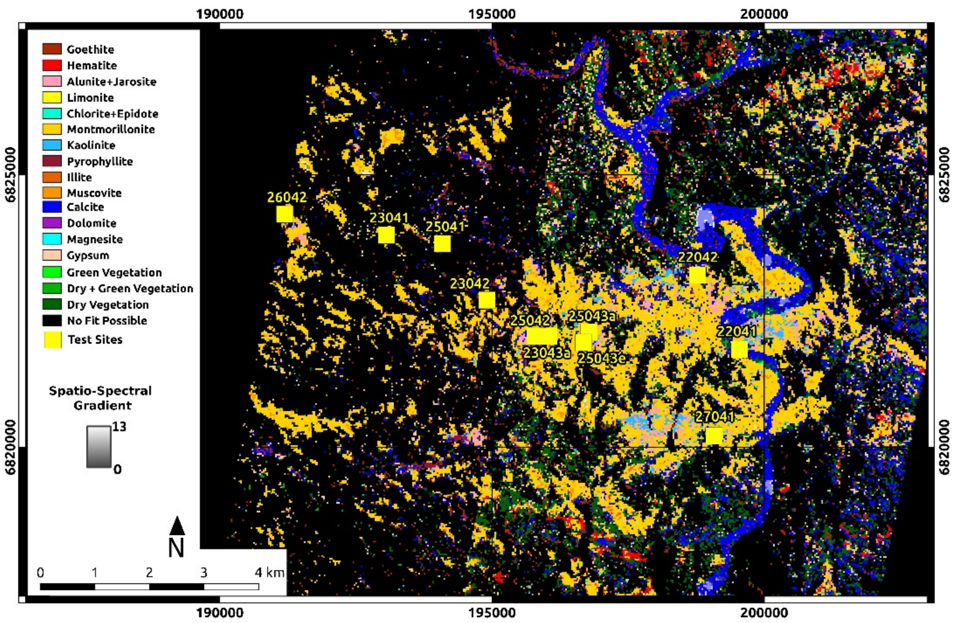

Figure S15. EnGeoMAP 2.0 result calculated from Hyperion data (EO1H1760802013267110KF and EO1H1760802014013110PF), using sensor dependent absorption depth thresholding. The semi-transparent overlay shows the spatio-spectral gradient. Prominent gradient edge pixel shown as non-transparent rim pixel around the semi-transparent gradient patches.

S5.3. Performance of EnGeoMAP 2.0 for Hyperion Data

Hyperion shows a high spectral performance, however, the results are generally lower than the results of the simulated EnMAP data averaging at 80%, as shown in Figure S16. Spatial performance averages at only 5% for the Hyperion data. Hyperion only shows 23% similarity to the Hymap reference. The difference in the spatial performance can be partially explained by the broader PSF of Hyperion and its lower SNR [6], if compared to EnMAP [7]. The lower mapping performance could also be explained by the low SNR of Hyperion. Here especially the low SNR values beyond 2000 nm cause a low material mapping performance of Hyperion, compared to the simulated EnMAP data.

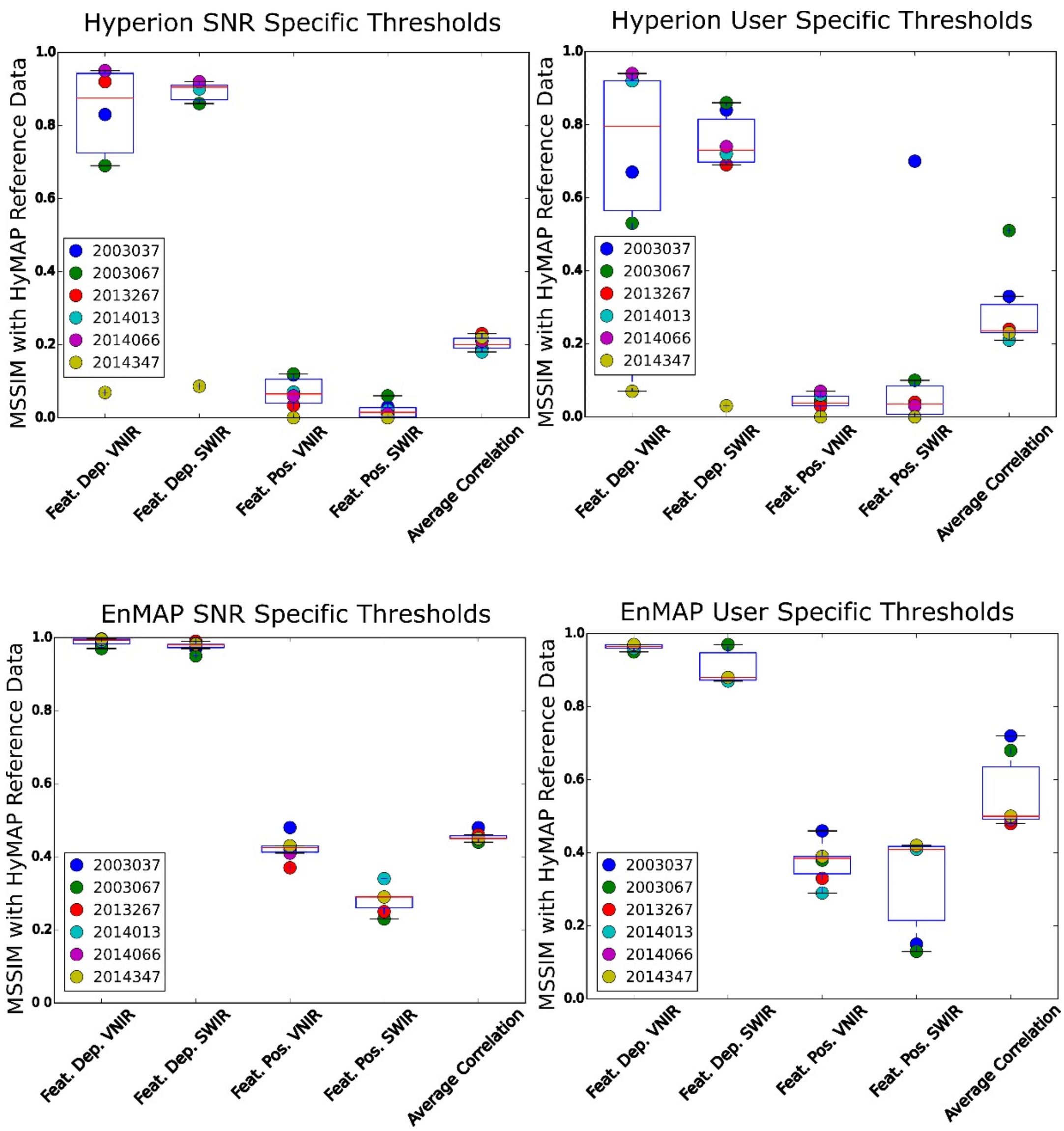

Figure S16. Comparison of the spectral (Feature Depth VNIR, Feature Depth SWIR), spatial (Feature Position VNIR, Feature Position SWIR) and material mapping performance (Average Correlation) at intersecting areas between the Hyperion data, simulated EnMAP data and the HyMAP reference data via the Mean Structural Similarity Index Measure. SNR specific thresholds depict the results from the sensor SNR specific EnGeoMAP 2.0 mapping approach, whilst the user specific thresholds depict the mapping results from fixed user defined absorption depth thresholds for the VNIR (2%) and the SWIR (3%).

Supplement 6

The here presented intrinsic validation results are EnGeoMAP 2.0 results calculated from simulated EnMAP data and ASD field spectra. Reference spectra from the USGS digital spectral library [9] and synthetic linear combinations labeled as mix have been used as reference spectra. Figure S17 shows results from the Rodalquilar area, whilst Figure S18 shows data from the Haib river complex.

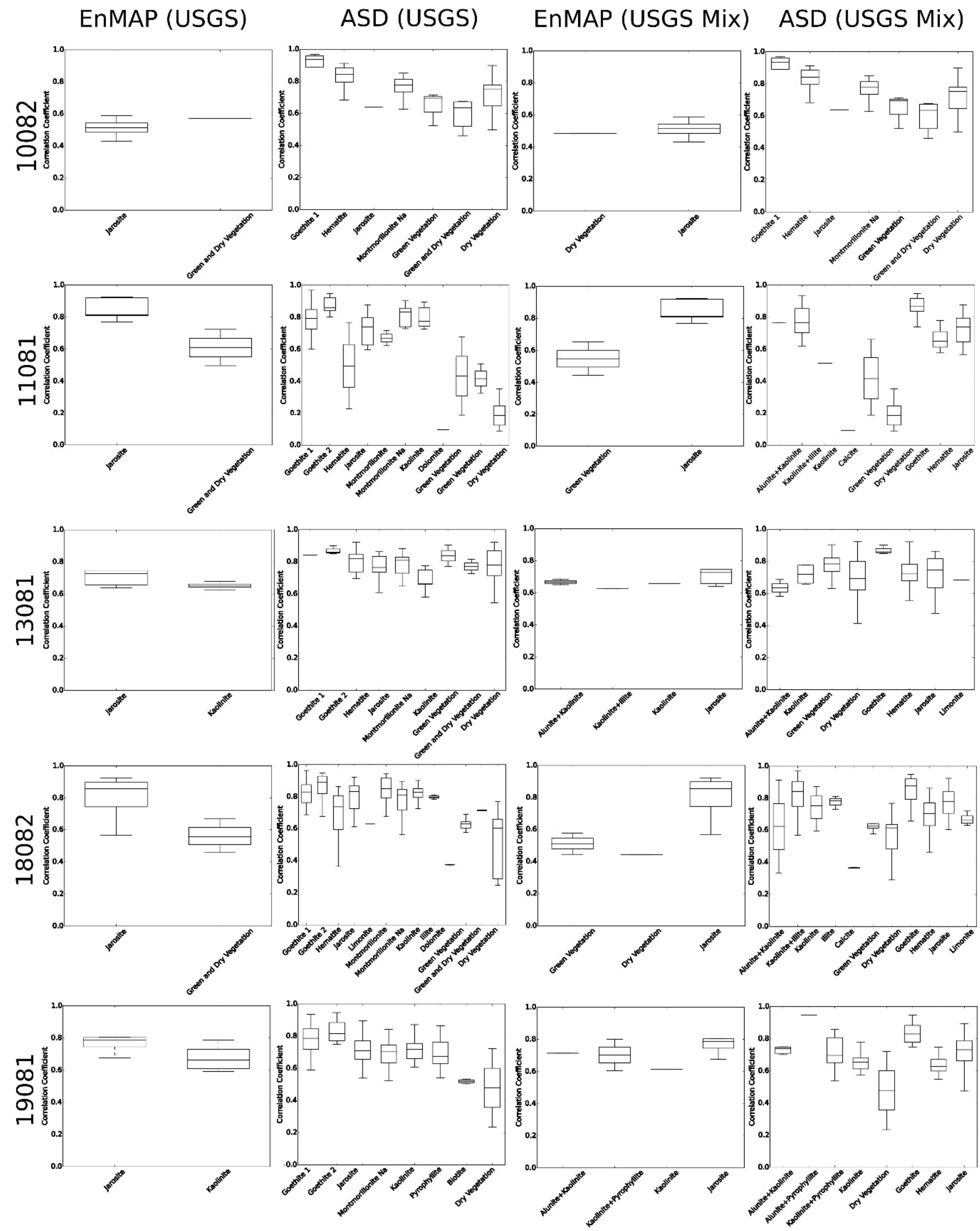

Figure S17. EnGeoMAP 2.0 correlation values calculated with reference spectra from the USGS digital spectral library and linear combinations thereof (e.g., Alunite+Kaolinite). The EnGeoMAP 2.0 results are calculated for simulated EnMAP data and ASD field spectroscopy data from the Rodalquilar area.

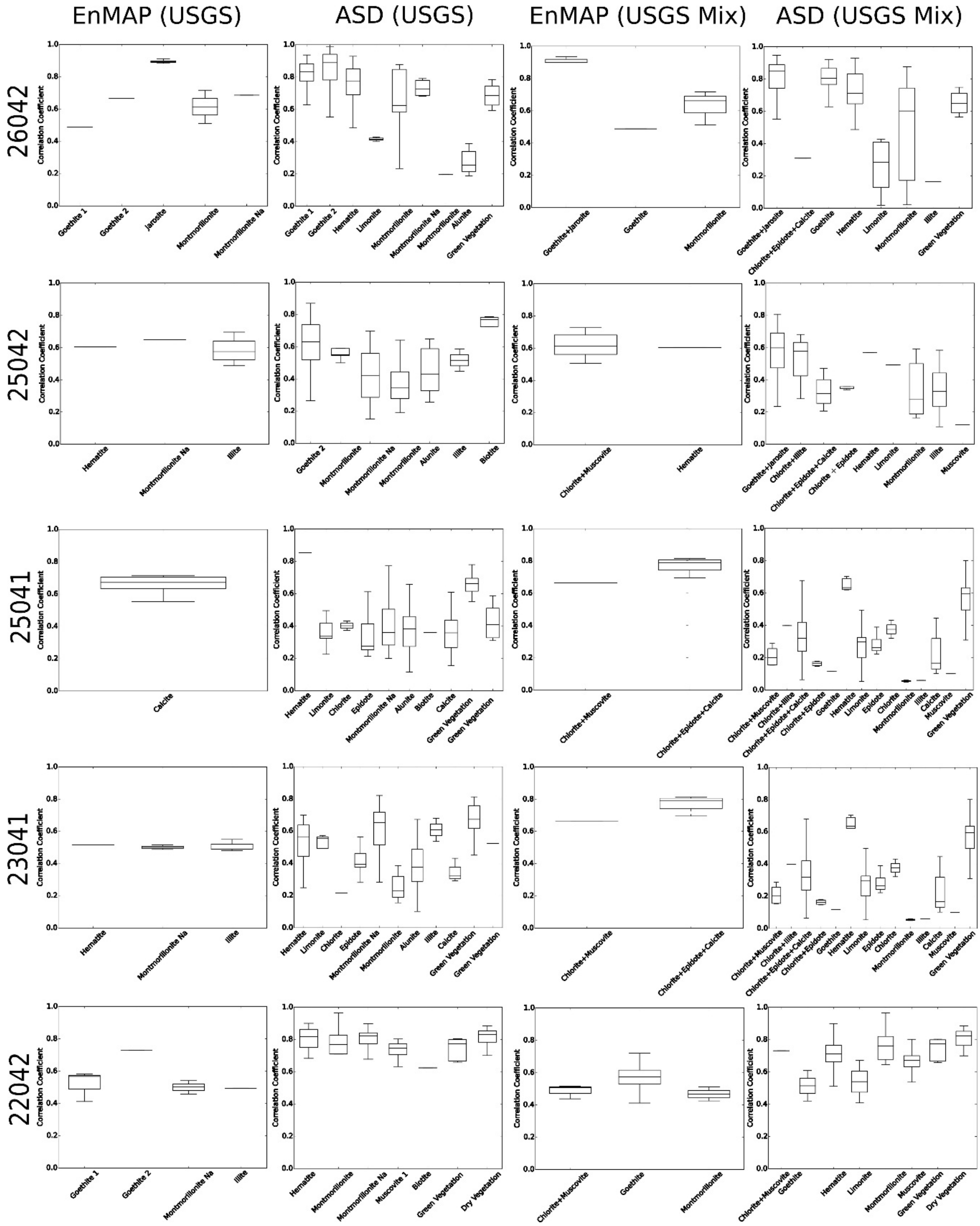

Figure S18. EnGeoMAP 2.0 correlation values calculated with reference spectra from the USGS digital spectral library and linear combinations thereof (e.g., Chlorite+Epidote + Calcite). The EnGeoMAP 2.0 results are calculated for simulated EnMAP data and ASD field spectroscopy data from the Haib River area.

References

1. Mielke, C.; Boesche, N.K.; Rogass, C.; Kaufmann, H.; Gauert, C. New geometric hull continuum removal algorithm for automatic absorption band detection from spectroscopic data. *Remote Sens. Lett.* **2015**, *6*, 97–105.
2. Papenfuß, A. Detection of Copper Deposits Based on a New Spectral Library Using Imaging Spectroscopy. Master's Thesis, Universität Potsdam, Potsdam, Germany, 2015.

3. Bannari, A.; Morin, D.; Bonn, F.; Huete, A.R. A review of vegetation indices. *Remote Sens. Rev.* **1995**, *13*, 95–120.
4. Minnitt, R.C.A. Porphyrry Copper-Molybdenium Mineralization at Haib River, South West Africa/Namibia. In *Mineral Deposits of Southern Africa Vol I&II*; Anhaeusser, C.R., Maske, S., Eds.; Geological Society of South Africa: Johannesburg, South Africa, 1986; Volume 2, pp. 1567–1585.
5. Barr, J.M.; Reid, D.L. Hydrothermal alteration at the Haib porphyry copper deposit, Namibia: Stable isotope and fluid inclusion patterns. *Commun. Geol. Surv. Namib.* **1993**, *8*, 23–34.
6. Pearlman, J.S. *Hyperion Validation Report*; Boeing Report; Phantom Works, The Boeing Company: Kent, WA, USA, 2003.
7. Guanter, L.; Kaufmann, H.; Segl, K.; Foerster, S.; Rogass, C.; Chabrillat, S.; Kuester, T.; Hollstein, A.; Rossner, G.; Chlebek, C.; *et al*. The EnMAP spaceborne imaging spectroscopy mission for earth observation. *Remote Sens.* **2015**, *7*, 8830–8857.
8. Middleton, E.M.; Ungar, S.G.; Mandl, D.J.; Ong, L.; Frye, S.W.; Campbell, P.E.; Landis, D.R.; Young, J.P.; Pollack, N.H. The Earth Observing One (EO-1) Satellite Mission: Over a decade in space. *IEEE J. Sel. Top. Appl. Earth Obs. Remote Sens.* **2013**, *6*, 243–256.
9. Clark, R.N.; Swayze, G.A.; Wise, R.; Livo, E.; Hoefen, T.M.; Kokaly, R.F.; Sutley, S.J. *USGS Digital Spectral Library Splib06a*; U.S. Geological Survey Data Series; U.S. Geological Survey: Denver, CO, USA, 2007.